Nuclear Materials Authority
P.O.Box 530 Maadi, Cairo, Egypt

ISSN 2314-5609
Nuclear Sciences Scientific Journal
8, 59- 78
2019
http:// www.ssnma.com

CONTRIBUTION TO THE GEOLOGY, PETROLOGY AND AIRBORNE GAMMA-RAY SPECTROMETRY OF GABAL EL-MUEILHA GRANITIC ROCKS, SOUTHERN EASTERN DESERT, EGYPT

ISMAIL M. ABDEL GHANI
Nuclear Materials Authority, P.O. 530 Maadi, Cairo, Egypt

ABSTRACT

Gabal (G.) El-Mueilha Granitic rocks are represented by an oval shaped stock that intruding the surrounding older rock units including ophiolitic mélange, metavolcanics, older granitoids and younger gabbros and sending several offshoots into them. The study area is affected by several fault systems in NW-SE, NE-SW and N-S directions. Petrographically, these younger granites are mainly represented by muscovite granite (syenogranite) that shows different degrees of albitization especially at the peripheral parts of the stock beside the ferrugination and silicification. The main accessory minerals are cassiterite, fluorite, zircon, beryl, monazite, thorite and uranothorite which are responsible for the radioactive anomalies in G. El-Mueilha syenogranitic mass. The airborne gamma ray spectrometry shows high radioactive anomaly restricted to the younger granitic mass relative to the other surrounding rocks that have low to moderate radioactivity. The eTh/eU ratio of G. El-Mueilha syenogranite indicates U-enrichment especially during albitization processes.

INTRODUCTION

The Arabian–Nubian Shield (ANS) is widely exposed tract of juvenile Neoproterozoic continental crust (1000–525 Ma) on Earth (Kröner, 1985; Stern, 1994; Johnson et al., 2011; Robinson et al., 2014) which are mainly formed by accretion of several intra-oceanic arcs along ophiolitic sutures (e.g. Kröner, 1985; Stoeser and Camp, 1985; Vail, 1985; Quick, 1991; Johnson, 1998; Stern and Johnson, 2010; Ali et al. 2009, 2010, 2016) . The Eastern Desert and Sinai are parts of the Nubian shield that comprises also eastern Sudan and Eritrea. The classification of granitoid rocks in the ANS include the syn- to late-orogenic granitoid assemblages (880–610 Ma), and post-orogenic to anorogenic granitoid assemblages (600–475 Ma), previously known as older granitoids and younger granites, respectively (Greenberg, 1981; Ries et al., 1983; Bentor, 1985; Stern and Hedge, 1985; Hassan and Hashad, 1990; Abdel-Rahman, 1995; Eliwa et al., 2006; Moussa et al., 2008 and Ali et al., 2012).

Gabal El-Mueilha younger granitic mass is considered as a topographic mark in the study area (703 m a.s.l.). It is located in the southern Eastern Desert, between latitudes 24° 51' and 24° 56' N and longitudes 33° 58' 10" and 34° 03' 50" E (Fig.1*)*. The early comprehensive petrological studies and geological mapping have been carried out and the granitic mass of G. El-Mueilha was a part of those studies (e.g. El-Ramly and El-Far, 1955*;* Soliman, 1981;

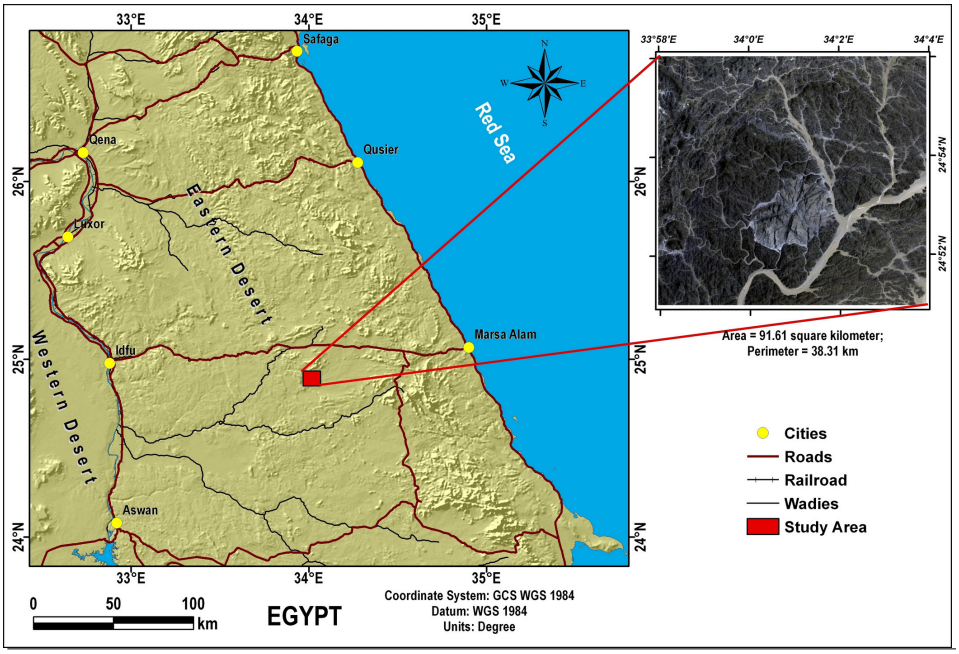

Fig.1: Location map of Gabal El Mueilha area, southern Eastern Desert, Egypt

Obeid et al., 2001; Badran, 2009; Samaan, 2009 and others). The present study deals with the geology, petrography, mineralogy and airborne spectrometry of the basement rocks in G. El Mueilha area with special emphases on the granitic rocks to indicate the factors controlling distribution of uranium and thorium. The importance of this study area regarded to the high radioactive anomaly that appears on the airborne spectrometric maps and the presence of rare metals as well as tin and fluorine mineralization in the rock association around G. El-Mueilha younger granites.

GEOLOGIC OUTLINE

A geologic map (scale 1:50000) for the study area is constructed by the aid of landsat-8 image processing as well as field work and the airborne spectrometric data (Fig.2). G. El-Mueilha is an oval-shaped stock of younger granites that characterized by high and rugged topography (703 m. a.s.l.), medium- to coarse-grained and light yellow to whitish buff or pink colours (Fig.3). It is characterized by well-developed vertical and nearly horizontal joints as well as the characteristic spheroidal exfoliation and cavernous weathering (Fig. 4) especially at the northern and northeastern roots of the pluton. G. El-Mueilha younger granites intrude the surrounding older rock units, which are mainly metavolcanics and ophiolitic mélange especially at Talat Um Hawd (Fig.5) and send several offshoots into them. Some huge offshoots from this pluton appears at El-Mueilha tin mine to the northwestern corner of the studied area (Fig.2).

The shared contacts between G. El-Mueilha granites and the metavolcanics are sharp intrusive and dip gently away from the granitic mass indicating its downward enlargement (Fig.6). Lithologically, these younger granites are mainly represented by muscovite

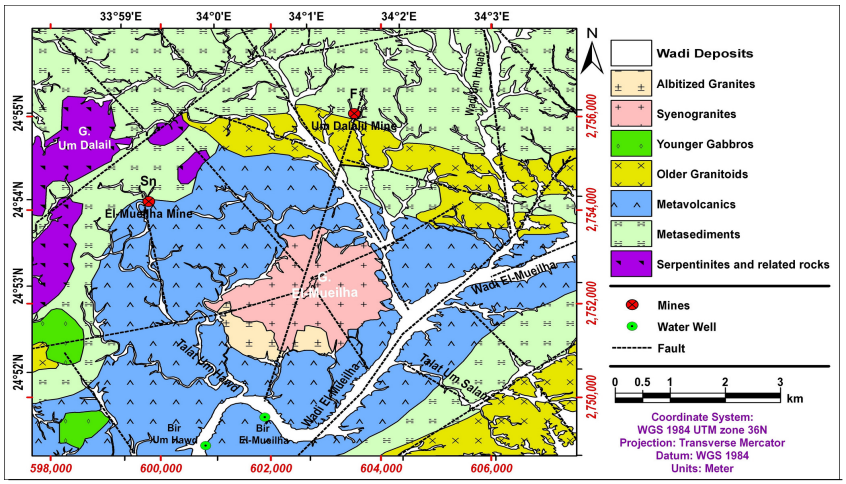

Fig.2: Geologic map of Gabal El Mueilha area, southern Eastern Desert, Egypt

Fig.3: Gabal El-Mueilha younger granites (YGR), showing high topography, intruding the surrounding rocks

Fig.4: Close up view showing cavernous and exfoliation weathering in Gabal El-Mueilha younger granites

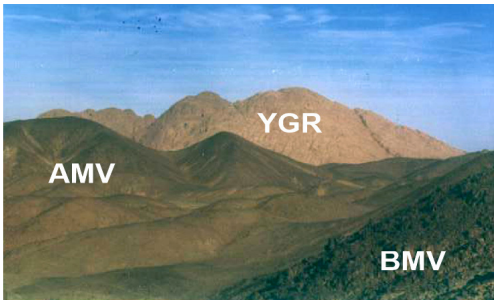

Fig.5: Gabal El-Mueilha younger granites (YGR) intruding both of felsic (AMV) and mafic (BMV) metavolcanics, looking east

Fig.6: Sharp intrusive contact, between the albitized younger granites (AYGR) and the metavolcanics (MV), dips gently away from the core of the granitic mass, looking north

granite that shows different degrees of albitization especially at the peripheral parts of the stock. The rock is whitish pink in colour and medium- to coarse-grained with characteristic feldspars phenocrysts. Different stages of alteration in G. El-Mueilha younger granites are encountered especially along fault and shearing planes comprising ferrugination and silicification. The number of the granitic offshoots increases near their contacts (Fig.7). Generally, El-Mueilha younger granites are intersected with numerous dykes of different thickness and attitudes; they range in composition from mafic to felsic ones (Fig.8) where the majority of them are mafic and showing lower topographic features. The study area is affected by several fault systems in NW-SE, NE-SW and N-S directions that more or less coincide with most wadis in the study area. Along some faults of them, many quartz and quartz with fluorite mineralization encountered such as at wadi Um Dalalil northeast the granitic mass.

PETROGRAPHY

Gabal El-Mueilha younger granites are mainly represented by muscovite granite that exhibits holocrystalline hypidiomorphic granular texture. The modal analysis (Table 1 and Fig.9*)* indicates that these younger granites fall in the syenogranite field of Streckeisen (1976).

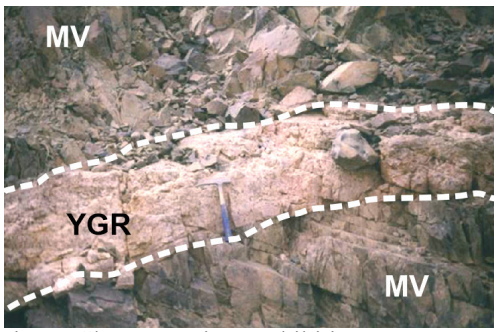

Fig.7: Close up view exhibiting a younger granitic offshoot cutting in the metavolcanics

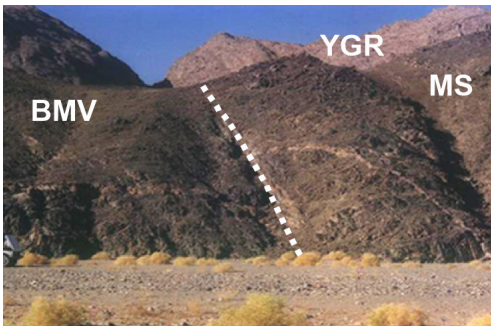

Fig.8: Normally faulted felsic dyke cutting in metavolcanics (BMV) and metasediments (MS), which in turn intruded by younger granites (YGR), looking west

Table 1: Modal analysis of Gabal El Mueilha granitic rocks, southern Eastern Desert, Egypt

Sample No.	1	2	3	4	5	6	7
Quartz	31.92	30.76	40.92	33.74	33.51	34.93	30.18
Alkali feldspar	45.04	48.69	39.89	49.24	46.24	43.75	51.28
Plagioclase	17.23	15.14	11.87	10.33	13.24	12.96	11.37
Muscovite	4.26	4.31	3.96	4.36	5.22	5.39	4.63
Biotite	0.24	1.15	0.87	1.16	0.94	2.14	1.08
Accessories	1.31	0.45	1.49	1.57	0.85	2.23	1.46
Total	100	100	100	100	100	100	100
Q	33.9	32.5	44.2	36.2	36.0	38.1	32.5
A	47.8	51.5	43.0	52.8	49.7	47.7	55.2
P	18.3	16.0	12.8	11.1	14.2	14.1	12.2

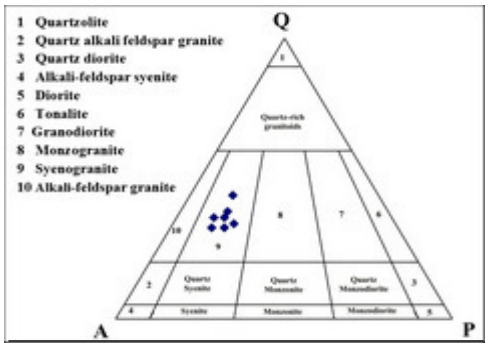

Fig.9: Q-A-P diagram according to the actual modal mineral constituents of Gabal El Mueilha granitic rocks, (After Streckeisen, 1976)

Syenogranites

G. El-Mueilha syenogranites are mainly composed of K-feldspars, quartz, plagioclase and muscovite in addition to biotite. Titanite, cassiterite, fluorite, apatite, zircon and opaques are accessories. ***Alkali feldspars*** are represented by orthoclase (up to 5 mm in length and 4 mm in width) and subordinate amounts of microcline showing various types of albite intergrowths including flame-like, patchy and string-like type (Fig.10). They enclosed several fresh plagioclase and quartz crystals in the form of poikilitic texture (Fig.11*)*. ***Quartz*** ranks second in abundance. It occurs as interstitial subhedral to anhedral crystals ranging in size from 0.2 mm to 3.5 mm across. Cracked quartz sometimes contains apatite, zircon, iron oxides and smaller plagioclase and quartz crystals as inclusions and is frequently dusted with iron oxides and clay minerals especially along peripheries and cracks (Fig.12*)*. Only few crystals show undulose extinction indicating that this rock is affected by stresses much lower than the other albitized younger granites. The cracked quartz crystals are very rare and are restricted to the fault planes. ***Plagioclase*** (An_{15} -An_{20}) occurs as subhedral to anhedral prismatic twinned crystals that sometimes show deformed twin lamellae (Fig.13). They are generally fresh

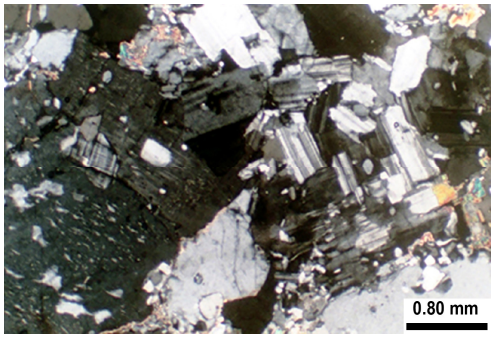

Fig.11: Fresh plagioclase and quartz crystals enclosed poikilitically in perthites, Gabal El-Mueilha syenogranite, XPL

Fig.12: Iron oxides and clay minerals filling cracked quartz crystals, Gabal El-Mueilha syenogranite, XPL

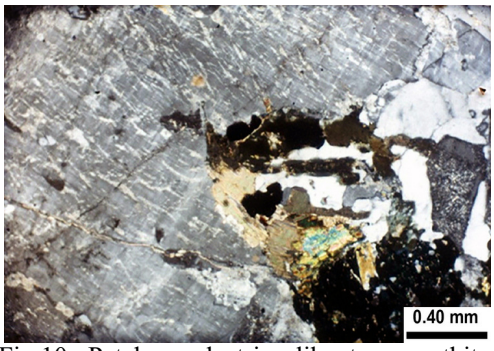

Fig.10: Patchy and string-like type perthite crystals corroded by quartz crystals, Gabal El-Mueilha syenogranite, XPL

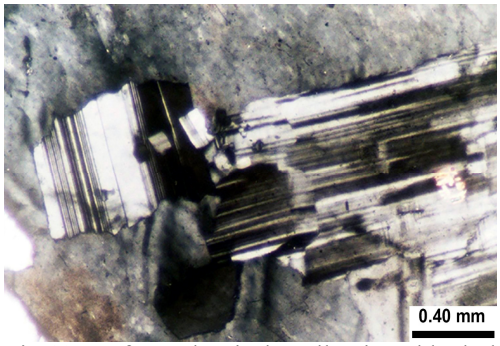

Fig.13: Deformed twin lamellae in subhedral prismatic plagioclase crystals, Gabal El-Mueilha syenogranite, XPL

and sometimes are slightly to moderately altered especially in their cores and along cracks. ***Muscovite*** occurs as medium, yellow, elongated, fan-shaped or leaf-like anhedral to subhedral interstitial flakes between other silicates. In addition, it includes subhedral prisms of plagioclase that dusted with fine inclusions along cleavage planes. Muscovite flakes also corrode and embay plagioclase and perthite crystals. Some muscovite flakes show pleochroic haloes (Figs. 14 and 15). They appear to be squeezed and deformed due to tectonic stresses or secondary growths of feldspars and quartz crystals reflecting the primary nature of muscovite. In some cases, minute muscovite flakes appear to be of secondary nature that filling the cracks. The presence of primary muscovite as inclusions in quartz or as large elongated flakes may reflect the peraluminous nature of this granite (Read,1984). ***Biotite*** occurs as subhedral to anhedral flakes. They are generally bleached and show one set of cleavages that traced with opaques due to alteration.

Opaques, titanite, apatite, fluorite and zircon are encountered as inclusions in silicates especially perthites, micas and quartz. Subhedral fine ***fluorite*** crystals are scattered all over the rock where the violet fluorite is engulfing anhedral grains of monazite and/or zircon. ***Zircon*** occurs in a very minor amount as subhedral to euhedral prismatic crystals as inclusions in muscovite and quartz. ***Titanite*** appears as anhedral to subhedral brown crystals, usually altered to magnetite and ilmenite along peripheries and cracks.

Along the shearing planes, the granite components are highly altered and fractured where quartz grains exhibit wavy extinction and plagioclase shows kinking and bending of the twinning lamellae.

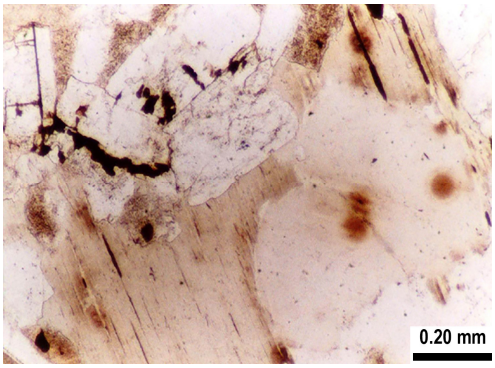

Fig.14: Muscovite flakes showing pleochroic haloes, Gabal El-Mueilha syenogranite, PPL

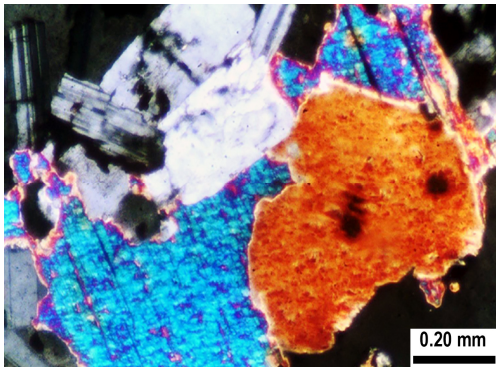

Fig.15: Muscovite flakes showing pleochroic haloes, Gabal El-Mueilha syenogranite, XPL

Albitized Syenogranites

The albitized syenogranites are similar in their mineral composition to the normal variety. They are mainly composed of plagioclase, quartz and K-feldspars, muscovite and lepidolite. Cassiterite, beryl, fluorite, apatite, zircon, monazite, thorite and uranothorite are accessories.

Plagioclase is the most dominant mineral. It occurs as anhedral to subhedral prismatic crystals ranging in size from 0.3 mm to 2.6 mm across. Some plagioclase crystals corrode each other indicating more than one plagioclase generation. This could be proved by the cracking and glide twinning and the core altered as well as the overgrowth zoning of some plagioclase crystals, while others show clear simple and lamellar twinning without

any sign of alteration. Some crystals represent a younger phase corroding other minerals, especially altered potash feldspars and plagioclase. Other crystals show zoning (Fig. 16), indicating local albitization (Peterson and Eliasson,1997).

Quartz exhibits undulose extinction and is highly cracked and mylonitized (Fig.17) indicating that they were subjected to high stresses (Read, 1984). The cracks are usually dusted with iron oxides and muscovite. Some quartz crystals show myrmekitic and graphic textures (Fig.18) with feldspars, suggesting reaction during crystallization (Read, 1984). The alkali feldspar crystals and plagioclases are usually serecitized (Figs.19 and 20) and replaced with albite due to albitization processes. Brown cassiterite crystals are also recorded especially in the sheared and greisenized granite (Fig. 21).

All over the peripheral zones of the granitic mass especially at El Mueilha tin mine as well as the main fault planes, the granite shows greisenization (El-Mansi,1996) that being partly or completely transformed into yellowish green rock composed of quartz, muscovite, yellow lepidolite, cassiterite and fluorite. Relics of biotite are also found in the muscovite flakes. Shearing effect is indicated

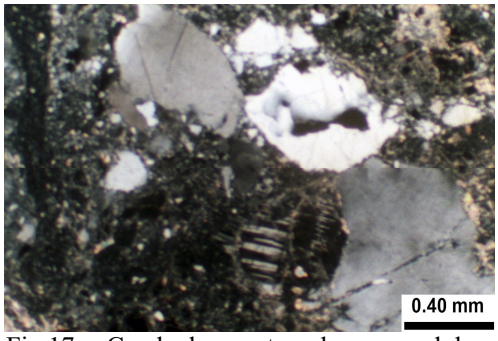

Fig.17: Cracked quartz shows undulose extinction, Gabal El Mueilha albitized granite, XPL

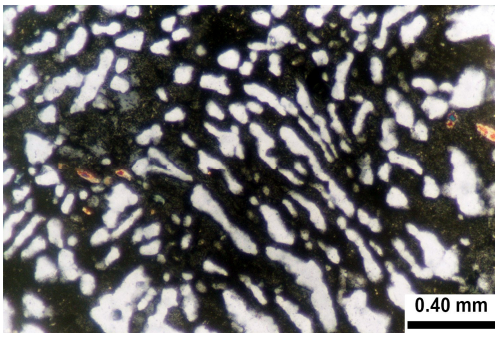

Fig.18: Quartz crystals show myrmekitic and graphic textures suggesting reaction during crystallization, Gabal El Mueilha albitized granite, XPL

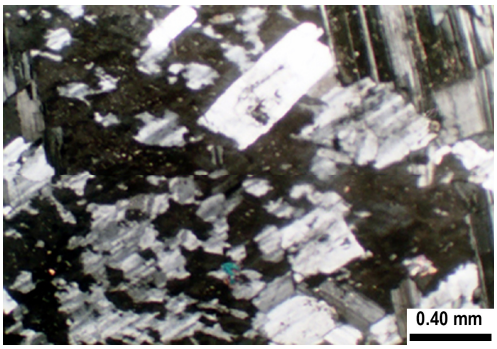

Fig.16: Younger phase of plagioclase crystals in optical continuity with the hosted perthite crystal, Gabal El Mueilha albitized granite, XPL

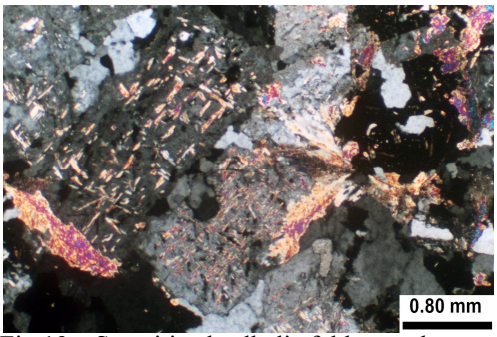

Fig.19: Serecitized alkali feldspar due to albitization processes, Gabal El Mueilha albitized granite, XPL

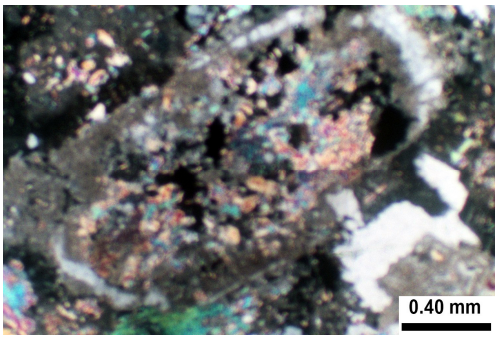

Fig.20: Serecitized plagioclase due to albitization processes, Gabal El Mueilha albitized granite, XPL

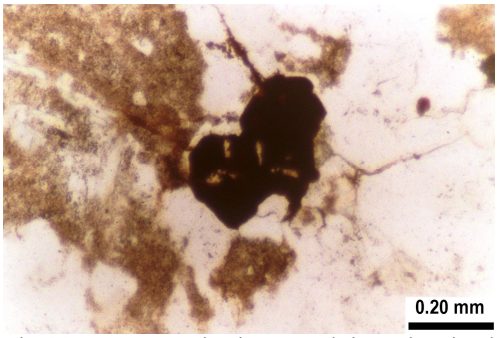

Fig.21: Brown cassiterite crystals in greisenized granite, Gabal El Mueilha albitized granite, PPL

by the bending of the twinning planes of plagioclase. Also, the crushing effect is mainly demonstrated along the crystal boundaries and by the undulose extinction of quartz. This indicates that the rock was subjected to shearing effects after the crystallization because the normal syenogranites do not suffer any valuable stresses. The micro-cracks are usually filled with quartz, iron oxides, muscovite and epidote.

MINERALOGICAL INVESTIGATION

Cassiterite (SnO_2)

Cassiterite is found in thin sections either from the granitic rocks or the quartz veins from El-Mueilha Tin mine as translucent subhedral prismatic crystals with brown to reddish brown colour. Zoning is common in most of the detected crystals. Some bipyramidal crystals found in some thin sections. Cassiterite is also identified by ESEM technique. EDAX shows 80 % or more Sn-content and some sort of chemical variation of cassiterite crystals from different samples (Fig.22).

Thorite and Uranothorite ($Th,U)(SiO_4$)

Thorite and uranothorite are found as subhedral prismatic crystals of yellow to brownish yellow colour, translucent to opaque. Sometimes, uranothorite is found as minute grains and as inclusions in other minerals especially muscovite, fluorite, and quartz (Fig. 23).

Fluorite (CaF_2)

Fluorite is found as irregular crystals of colourless to purple colour in thin sections. In the hand specimens, green and violet grains can be detected by hand lens. The variable colouration of fluorite was a matter of previous intensive studies that attribute this phenomenon to many reasons such as; impurities, REE contents, Y and Sr contents or/and radiation that cause physical distortion in crystal structure (Deer et al.,1992; El-Mansi, 2000; Raslan, 2009). Inclusions inside some fluorite grains show high U and Th contents. These inclusions are mainly of monazite, uranothorite and thorite (Fig.24). This is confirmed by ESEM (Fig.25).

Beryl [$Be_3Al_2(SiO_3)_6$]

Beryl is found as subhedral to euhedral colourless prismatic to tabular crystals (Fig.26). Most of the defined beryl grains were found in the albitized samples and rarely detected in the non albitized syenogranites. Some equant crystals were also recorded in the albitized granites.

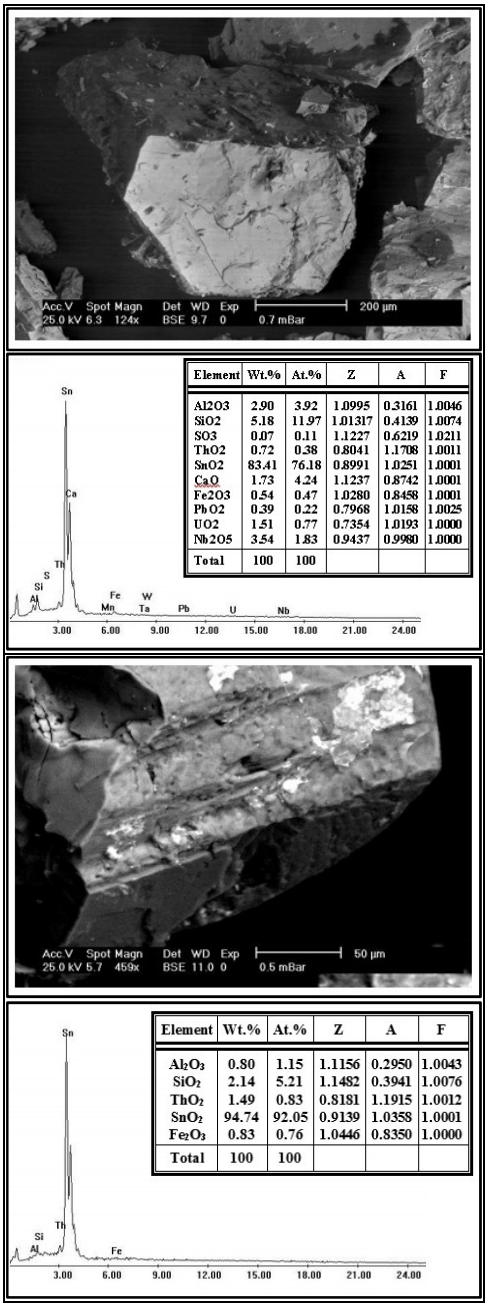

Element	Wt.%	At.%	Z	A	F
Al2O3	2.90	3.92	1.0995	0.3161	1.0046
SiO2	5.18	11.97	1.01317	0.4139	1.0074
SO3	0.07	0.11	1.1227	0.6219	1.0211
ThO2	0.72	0.38	0.8041	1.1708	1.0011
SnO2	83.41	76.18	0.8991	1.0251	1.0001
CaO	1.73	4.24	1.1237	0.8742	1.0001
Fe2O3	0.54	0.47	1.0280	0.8458	1.0001
PbO2	0.39	0.22	0.7968	1.0158	1.0025
UO2	1.51	0.77	0.7354	1.0193	1.0000
Nb2O5	3.54	1.83	0.9437	0.9980	1.0000
Total	100	100			

Element	Wt.%	At.%	Z	A	F
Al_2O_3	0.80	1.15	1.1156	0.2950	1.0043
SiO_2	2.14	5.21	1.1482	0.3941	1.0076
ThO_2	1.49	0.83	0.8181	1.1915	1.0012
SnO_2	94.74	92.05	0.9139	1.0358	1.0001
Fe_2O_3	0.83	0.76	1.0446	0.8350	1.0000
Total	100	100			

Fig.22: Scanning electron microscope images and its EDAX table for cassiterite crystals of Gabal El-Mueilha granites

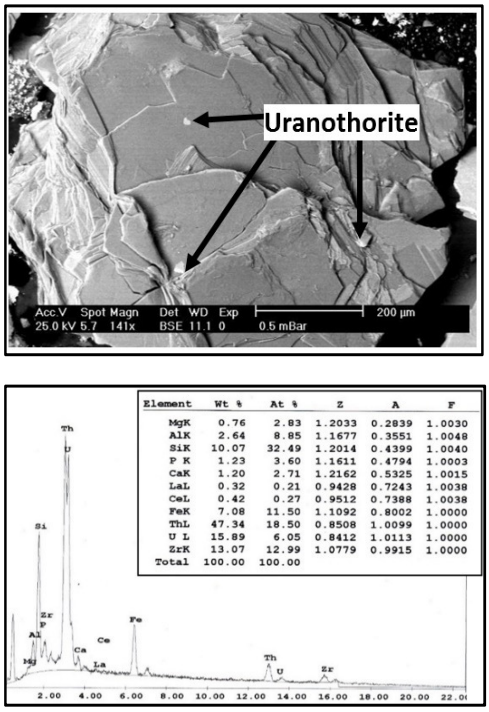

Element	Wt %	At %	Z	A	F
MgK	0.76	2.83	1.2033	0.2839	1.0030
AlK	2.64	8.85	1.1677	0.3551	1.0048
SiK	10.07	32.49	1.2014	0.4399	1.0040
P K	1.23	3.60	1.1611	0.4794	1.0003
CaK	1.20	2.71	1.2162	0.5325	1.0015
LaL	0.32	0.21	0.9428	0.7243	1.0038
CeL	0.42	0.27	0.9512	0.7388	1.0038
FeK	7.08	11.50	1.1092	0.8002	1.0000
ThL	47.34	18.50	0.8508	1.0099	1.0000
U L	15.89	6.05	0.8412	1.0113	1.0000
ZrK	13.07	12.99	1.0779	0.9915	1.0000
Total	100.00	100.00			

Fig.23: Scanning electron microscope image and its EDAX table for uranothorite inclusions in muscovite flake of Gabal El Mueilha granites

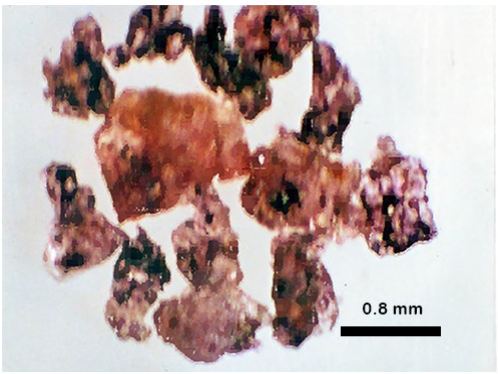

Fig.24: Violet fluorite grains including thorite and uranothorite inclusions

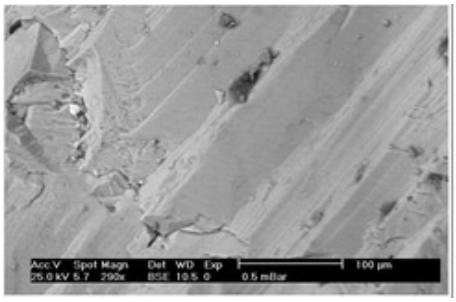

Element	Wt.%	At.%	Z	A	F
F_2O	34.91	36.18	0.9826	0.1237	1.0002
SrO	0.12	0.06	0.8337	0.8474	1.0092
ThO_2	0.53	0.11	0.6932	1.4126	1.0093
UO_2	0.70	0.14	0.6981	0.9013	1.0081
CaO	63.58	63.44	0.9787	0.9897	1.0001
Fe_2O_3	0.17	0.06	0.8973	0.9361	1.0000
Total	100	100			

Fig.25: Scanning electron microscope image and its EDAX table for fluorite of Gabal El Mueilha granites

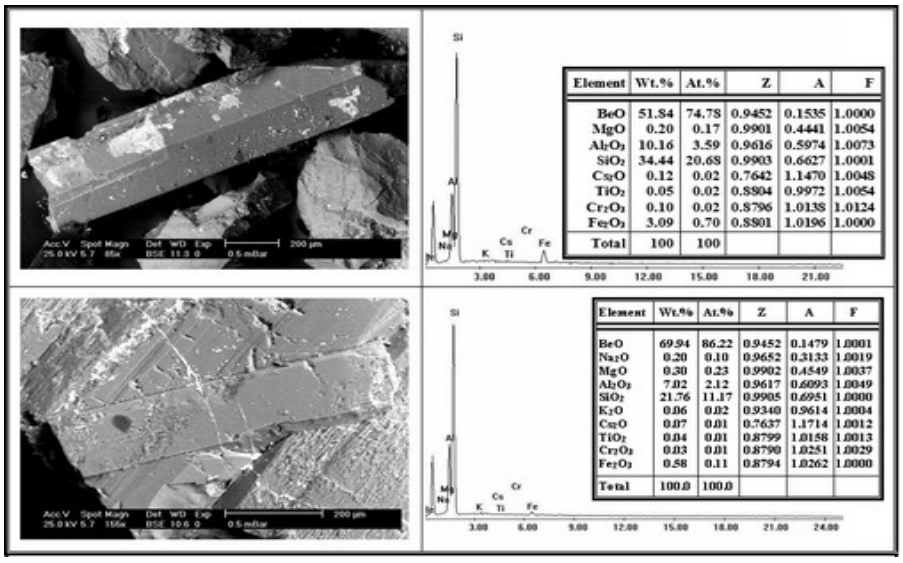

Element	Wt.%	At.%	Z	A	F
BeO	51.84	74.78	0.9452	0.1535	1.0000
MgO	0.20	0.17	0.9901	0.4441	1.0054
Al_2O_3	10.16	3.59	0.9616	0.5974	1.0073
SiO_2	34.44	20.68	0.9903	0.6627	1.0001
Cs_2O	0.12	0.02	0.7642	1.1470	1.0048
TiO_2	0.05	0.02	0.8804	0.9972	1.0054
Cr_2O_3	0.10	0.02	0.8796	1.0138	1.0124
Fe_2O_3	3.09	0.70	0.8801	1.0196	1.0000
Total	100	100			

Element	Wt.%	At.%	Z	A	F
BeO	69.94	86.22	0.9452	0.1479	1.0001
Na_2O	0.20	0.10	0.9652	0.3133	1.0019
MgO	0.30	0.23	0.9902	0.4549	1.0037
Al_2O_3	7.02	2.12	0.9617	0.6093	1.0049
SiO_2	21.76	11.17	0.9905	0.6951	1.0000
K_2O	0.06	0.02	0.9340	0.9614	1.0004
Cs_2O	0.07	0.01	0.7637	1.1714	1.0012
TiO_2	0.04	0.01	0.8799	1.0158	1.0013
Cr_2O_3	0.03	0.01	0.8790	1.0251	1.0029
Fe_2O_3	0.58	0.11	0.8794	1.0262	1.0000
Total	100.0	100.0			

Fig.26: Scanning electron microscope image and its EDAX table for beryl of Gabal El Mueilha granites

Zircon ($ZrSiO_4$)

Zircon occurs as subhedral to euhedral colourless prismatic crystals in thin sections. Some grains are metamicted due to radiation damage. It contains significant amount of Th due to the replacement of Zr by Th forming thorite ($ThSiO_4$). There is a clear intergrowth between zircon and thorite due to the close-up similarity of the ionic radii of Zr and Th (Omran and Dessouky, 2016). Also, zircon occurs as inclusions in muscovite flakes (Fig.27).

Monazite (Ce, La, Nd, Th)PO_4

Monazite occurs in the studied granites as an accessory mineral associated with zircon and uranothorite. Here it is found as inclusions in muscovite flakes (Fig.27).

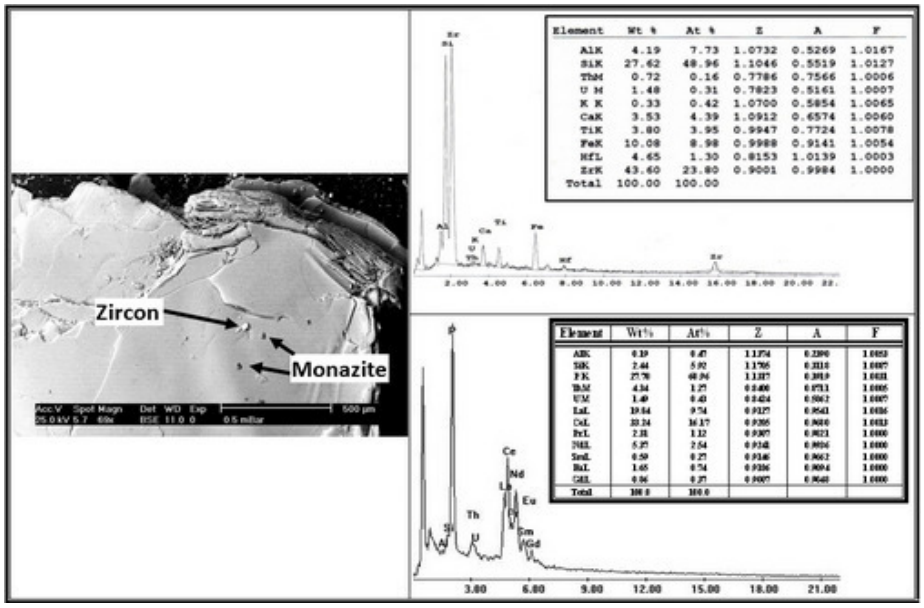

Fig.27: Scanning electron microscope image and its EDAX table for zircon and monazite inclusions in muscovite flakes of Gabal El Mueilha granites

AIRBORNE GAMMA-RAY SPECTROMETRY

Airborne gamma-ray spectrometry originally developed as a tool for uranium exploration but this tool usage has been extended to include mineral exploration and geologic mapping (Grasty and Shives, 1997; Elsirafy et al., 1999: Fouad et al., 2004; Hyvönen et al., 2005; Khamies and Terras, 2009; Aboelkhair et al., 2014; Badr, 2017; Dawoud et al., 2017). Airborne gamma-ray spectrometry measures the abundance of potassium, thorium and uranium in rocks and weathered materials by detecting gamma-ray emitted due to the natural radioelement decay of these elements. The airborne survey of the study area was carried out by Aero-Service Division of the Western Geophysical Company of America in 1984. Spectral radiometric measurements were made using high-sensitivity 256-channel airborne gamma-ray spectrometer with a primary 50.3 liters sodium iodide, thallium activated (NaI "TI") detector array, (Aero-Service, 1984). The data generated from the flight line profiles were corrected for background radiation, and for Compton scattered gamma-rays in the potassium and uranium energy window. The corrected data are processed using Geosoft Oasis Montaj software (version 8.4) resulting in filled coloured maps that are subjected to qualitative and quantitative interpretations. All the aero-spectrometric data (TC, K, eU, and eTh values) are multiplied by 10. However, the studied area shows a very high positive anomaly which attracted the attention of many researchers.

Qualitative Interpretation of the Airborne Gamma-ray Spectrometric Data.

Radioelements contour maps comprising (eU in ppm), (eTh in ppm), (K in %) in addition to the total count (TC in μr) are shown on Figures. 28-31. The interpretation of radioelements distribution for mapping the surface geology is based on the fact that each rock type

has its own rock-forming minerals with certain amounts, which comprise specific quantities of radioactive elements (Elawadi et al., 2004). The radioelements concentration can be attributed either to primary mineralization events or to secondary processes. The higher degree of weathering may produce a distinctive gamma-ray response compared with the surrounding bedrock (Wilford, 1992).

Radioelements contour maps

The equivalent uranium (eU) content reaches up to 140 ppm, as a maximum value over younger granites, and diminishes to 3 ppm as a minimum value over ophiolitic mélange (serpentinites and metasediments). The eU contour map (Fig.28) can be classified into three levels. The first level expands from 15 ppm up to 140 ppm and is essentially associated with G. El Mueilha younger granites, some areas of the older granitoids and the metavolcanics where younger granitic offshoots occurred cutting through the older granitoids and metavolcanics. The intermediate level ranges from 10 to 15 ppm and is associated mainly with older granitoids, metavolcanics and wadi deposits. The low levels with values less than 10 ppm, extend over the ophiolitic mélange comprising serpentinites, talc carbonates and metasediments.

The eTh contour map (Fig.29) shows that both the normal and albitized syenogranites and small parts of the metavolcanics have highest values in the study area, 222, 121 and 120 ppm, respectively. Besides, the eTh contour map can be divided into three levels. The first level has eTh contents more than 35 ppm and is essentially associated with the younger granites and areas with offshoots from them cutting in the metavolcanics. The second level ranges from 25 to 35 ppm and is restricted to wadi deposits and older granitoids. The low-level is lower than 25 ppm, which is mostly associated with ophiolitic mélange and metavolcanics.

The K contour map (Fig.30) shows the overall spatial distribution of the relative potassium concentrations in the study area. It indicates that serpentinites and related rocks represent the low level (less than 7 %); while the intermediate level ranges from 7 to 10 percent, which is associated with the older granitoids and metavolcanics. The high level (>10 %) is associated with younger granites

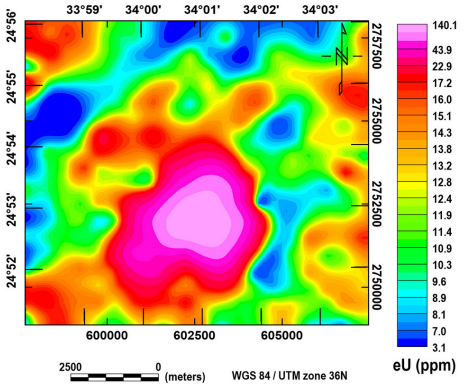

Fig.28: Uranium contour map (eU in ppm)of Gabal El Mueilha area, Southern Eastern Desert, Egypt

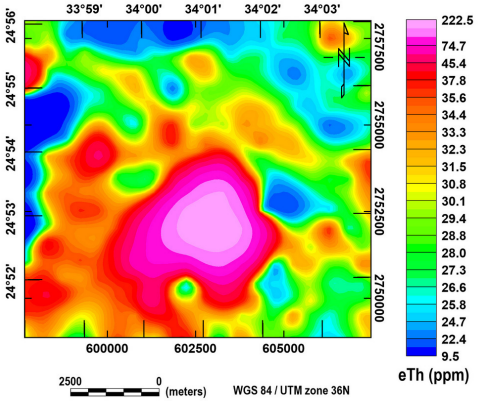

Fig.29: Thorium contour map (eTh in ppm)of Gabal El Mueilha area, Southern Eastern Desert, Egypt

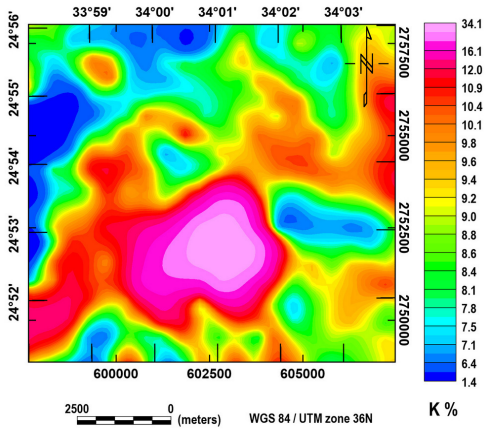

Fig.30: Potassium contour map (K%) of Gabal El Mueilha area, Southern Eastern Desert, Egypt

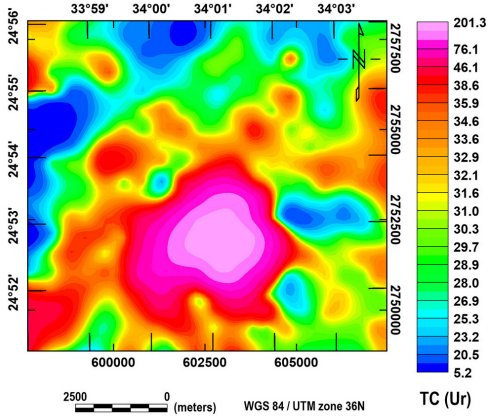

Fig.31: Total-count radiometric contour map (TC in µr) of Gabal El Mueilha area, Southern Eastern Desert, Egypt

and some areas of the older granitoids, as well as the metavolcanics affected by the younger granites offshoots.

The TC map (Fig.31) shows three radiometric levels, high, intermediate and low. The high level indicates values exceeding 35 µr. This level is observed over younger granites and the areas affected by their offshoots in the surrounding metavolcanics. The intermediate level ranges from 28 to 35 µr and is mainly associated with the older granitoids and metasediments as well as wadi deposits. The low level, varies from 5 to 28 µr, and extends over ophiolitic mélange rocks especially serpentinites and metasediments rich in blocks and fragments of serpentinites.

From the above interpreted radioelements and TC coloured maps, it is clear that the ophiolitic mélange rocks (serpentinites and metasediments), the metavolcanics and younger gabbros exhibit low radioactivity levels in the study area. Meanwhile, the metavolcanics are of wide range in radioactivity due to their close vicinity to the younger granitic mass and the common presence of many offshoots of the younger granites inside them as well as the younger granitic debris flown along wadis and tributaries surrounding G. El-Mueilha younger granites. The older granitoids are of intermediate radioactivity relative to the different rock units exposed in the study area. In general, the anomalous rock unit from the radioactivity point of view, is the younger granites of G. El Mueilha.

Composite images

The following composite images are developed by the USGS (Duval, 1983) comprising: a) The radioelements composite image including K, eTh and eU in RGB (Red, Green and Blue) respectively; b) The potassium composite image including K, (K/eTh) and (K/eU) in RGB; c) The uranium composite image including eU, (eU/eTh) and (eU/K) in RGB and d) The thorium composite image including eTh, (eTh/eU) and (eTh/K) in RGB (Figs.32-35).

The radioelements composite image clarified the high concentration of K, eTh and eU (white colour) is great correlated with the spread of only G. El-Mueilha syenogranites

with few exception areas (metavolcanics with intensive granitic offshoots and wadis with younger granitic debris) such as the area to the northwest and southwest of G. El-Mueilha (Fig. 32).

The potassium composite image (Fig. 33) exhibits that the highest K-concentration (strong red) is only associated with the fresh granites of G. El-Mueilha whereas the albitized variety is relatively lower in K-content. Also, this image shows a minor spot with high K-concentration to the northwest of G. El-Mueilha younger granites around El-Mueilha tin mine where there are a lot of younger granitic offshoots cutting through the metavolcanics and/or the role of the hydrothermal solutions that responsible for forming tin mineralization.

The uranium composite image (Fig. 34) shows that the lowest eU-concentration (dark black) is associated mainly with mafic and ultramafic rock varieties of the ophiolitic mélange and younger gabbros as well as mafic metavolcanics (scattered all over the area especially north and west of the map) whereas the highest eU-concentration (white) associated with G. El-Mueilha younger granites.

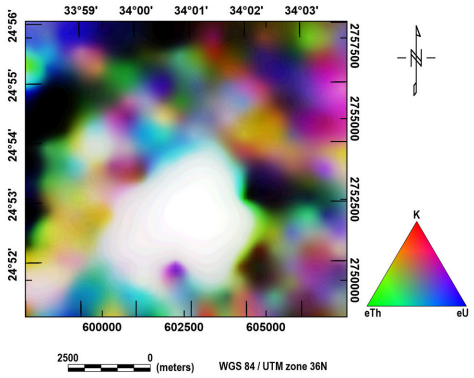

Fig.32: Radioelements composite image ternary map of Gabal El Mueilha area, Southern Eastern Desert, Egypt

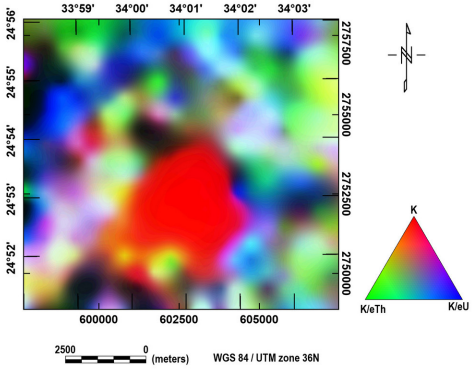

Fig.33: Potassium composite image ternary map of Gabal El Mueilha area, Southern Eastern Desert, Egypt

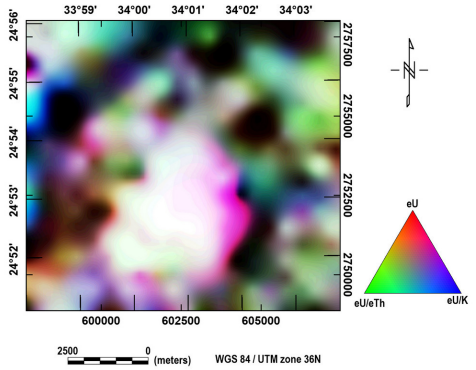

Fig.34: Uranium composite image ternary map of Gabal El Mueilha area, Southern Eastern Desert, Egypt

The thorium composite image (Fig.35) emphases the relative distribution of thorium and highlights area of thorium enrichment. The highest eTh-concentrations (red colour) shown at the southwestern periphery of G. El-Mueilha and associated with the albitized granites. However, the fresh granites are relatively lower in Th-content (magenta colour). The lowest eTh-concentrations (black colour) shown at the northeastern and northwestern

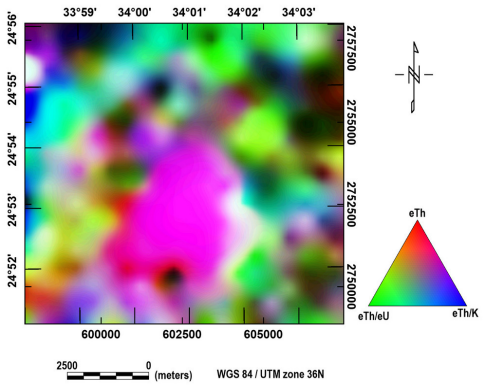

Fig.35: Thorium composite image ternary map of Gabal El Mueilha area, Southern Eastern Desert, Egypt

corners of the map associating with the ophiolitic mélange rocks.

Quantitative Interpretation of the Airborne Gamma-ray Spectrometric Data

Th/U ratios for granitic rocks are thought to be normal if they are within the range of 3 to 5, (Nash, 1979; Stuckless, 1979). The minimum, maximum and average of the K%, eU (ppm) and eTh (ppm) as well as their ratios eTh/eU of each rock unit exposed in the study area are shown in Table (2) and Fig. (36). The radioelements values of each rock type are nearly consistent with the normal averages of eU in contrast with eTh where they are of slight uranium addition. The metavolcanics

Table 2: K%, eU, eTh and eTh/eU of the different rock units, Gabal El-Mueilha area, Southern Eastern Desert, Egypt

Rock type			K %	eU (ppm)	eTh (ppm)	eTh/eU
Younger granites	Albitized Syenogranites	Minimum	19	50	80	1.2
		Maximum	26.0	100.0	122	1.6
		Average	22.5	69.8	101.3	1.5
	Syenogranites	Minimum	13	35	80	1.2
		Maximum	34	140	222	2.7
		Average	24.6	92.5	155.9	1.8
Younger Gabbros		Minimum	6.0	9.0	25.0	1.9
		Maximum	11.6	19.0	40.0	4.0
		Average	9.5	13.2	33.8	2.8
Older Granitoids		Minimum	7.9	6.0	22.0	1.6
		Maximum	10.8	16.0	33.0	5.2
		Average	9.2	12.4	28.6	2.4
Metavolcanics		Minimum	6.7	6.0	23.0	1.1
		Maximum	24.0	80.0	150.0	4.5
		Average	9.9	17.0	37.4	2.4
Ophiolitic mélange	Metasediments	Minimum	5.0	5.0	19.0	1.4
		Maximum	13.0	20.0	42.0	5.4
		Average	8.8	11.6	29.0	2.6
	Serpentinites	Minimum	2.5	4.0	12.0	1.7
		Maximum	9.1	11.0	33.0	5.5
		Average	5.7	7.7	22.4	3.1

"The measured TC, K, eU, and eTh values are multiplied by 10"

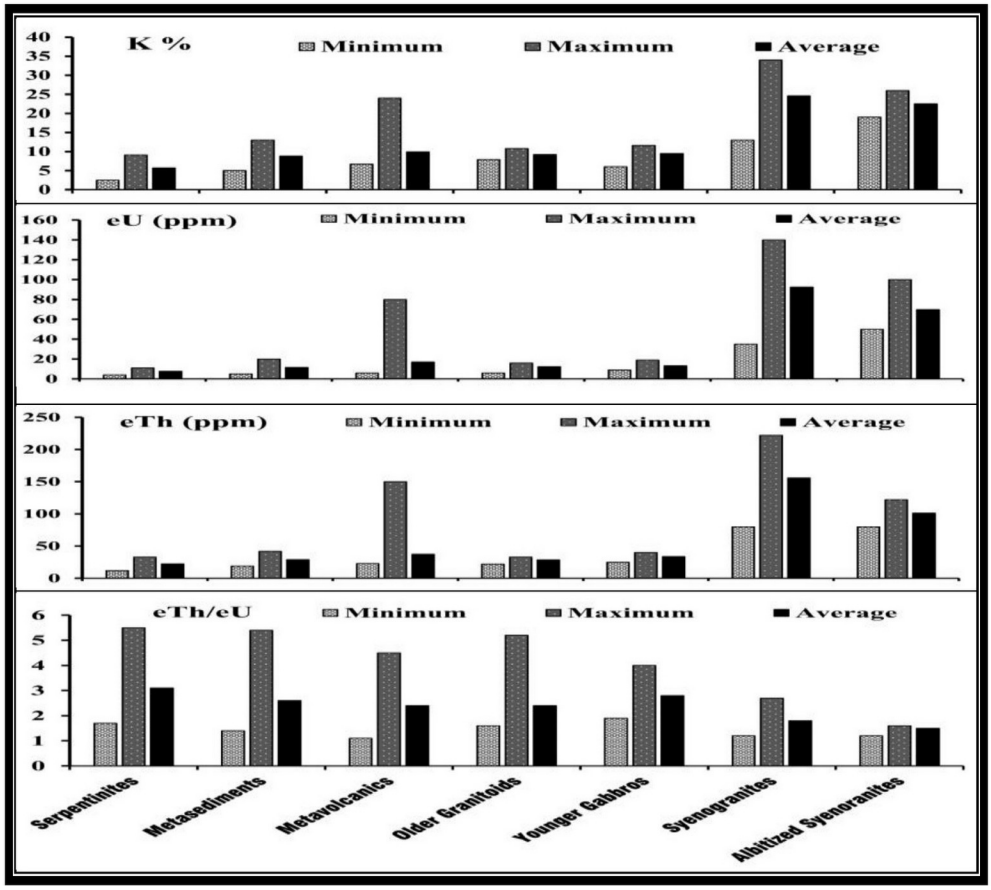

Fig.36: Bar diagrams for the minimum, maximum and averages of K%, eU, eTh and eTh/eU in the different rock types of G. El Mueilha area, Southern Eastern Desert, Egypt. (The measured K, eU, and eTh values are multiplied by 10)

show relative high values of K, eU and eTh due to its vicinity with the younger granites and the common presence of younger granitic offshoots into them. The albitized syenogranites show common lower eTh/eU values than the normal syenogranites indicating uranium addition or enrichment due to hydrothermal processes.

CONCLUSIONS

El-Mueilha crops out as an oval shaped syenogranitic mass elevated 703 m (a.s.l.) and represent a good landmark in the area that covered by other low-lying basement rocks (Ophiolitic mélange, metavolcanics, older granitoids and younger gabbros). The usage of landsat-8 image processing and field work delineated the albitization zones of the syenogranitic mass and precisely defined the contact lines between the different rock units as well as the alteration zones. The main alterations in G. El-Mueilha syenogranitic mass are

ferrugination, silicification and albitization, which are restricted to the fault planes as well as the peripheral parts of the pluton along their contacts with the surrounding metavolcanics. The airborne Gamma-ray spectrometry shows a high anomaly restricted to the syenogranitic mass compared with the other surrounding rocks. Petrographic and mineralogical studies indicated that the high uranium content of G. El-Mueilha syenogranites is attributed to the presence of zircon, monazite, thorite and uranothorite. Beryl is found, for the first time in G. El-Mueilha granitic mass, in both albitized and non-albitized syenogranites. The equant variety of beryl only detected in the albitized syenogranites. Cassiterite and fluorite are not only encountered as discrete crystals in the main syenogranitic mass but also as their own mineralizations away from the mass where cassiterite mineralization occurs at El-Mueilha tin mine about 3 km northwest the main granitic mass and fluorine mineralization at Um Dalalil mine about 2 km northeast of the main granitic mass. The close relation of these mineralizations to the granitic mass suggesting that the magmatic and the subsequent alteration processes play the most important role in formation of these mineralizations.

REFERENCES

Abdel-Rahman, A.M., 1995. Tectonic-magmatic stages of shield evolution: The Pan-African belt in northeastern Egypt. Tectonophysics, 242, 223– 240.

Aboelkhair, H.; Hasan, E., and Sehsah, H., 2014. Mapping of Structurally Controlled Uranium Mineralization in Kadabora Granite, Central Eastern Desert, Egypt Using Remote Sensing and Gamma Ray Spectrometry Data. The Open Geology J., 8, (Suppl 1: M4), 54-68.

Aero Service, 1984. Final operational report of airborne magnetic/ radiation survey in the Eastern Desert, Egypt, for the Egyptian General Petroleum cooperation. Aero Service, Houston, Texas, April, 1984, six volumes.

Ali, K.A.; Azer, M.K.; Gahlan, H.A.; Wilde, S.A.;Samuel, M.D., and Stern R.J., 2010. Age constraints on the formation and emplacement of Neoproterozoic ophiolites along the Allaqi-Heiani Suture, South Eastern Desert of Egypt. Gond. Res., 18,583–595

Ali, K.A.; Basem, A.Z.; Stern, R.J.; Andresen, A.; Martin, J.W., and Wagih, W.B., 2016. Lu–Hf and O isotopic compositions on single zircons from the North Eastern Desert of Egypt, Arabian–Nubian Shield. Implications for crustal evolution Gondwana Research ,32,181–192,

Ali, K.A.; Moghazi, A.M.; Maurice, A.E.; Omar, S.A.; Wang, Q.; Wilde, S.A.; Moussa, E.M.; Manton, W.I., and Stern, R.J., 2012. Composition, age, and origin of the ≈620 Ma Humr Akarim and Humrat Mukbid A-Type granites: no evidence for pre-Neoproterozoic basement in the Eastern Desert, Egypt. Int. J. Earth Sci., 101, 1705–1722.

Ali, K.A.; Stern, R.J.; Manton, W.I.;Kimura, J.I., and Khamees, H.A., 2009. Geochemistry, Nd isotopes and U-Pb SHRIMP dating of Neoproterozoic volcanic rocks from the Central Eastern Desert of Egypt: new insights into the 750 Ma crust-forming event. Precamb. Res., 171,1–22.

Badr, Y.S., 2017. Application of remote sensing technique in geologic mapping of hydrothermal alteration zones and possible radioactive potentialities at Ras Barud - Um Tagher area, North Eastern Desert, Egypt. Ph.D. Thesis, Fac. Sci., Menoufiya Univ., Egypt, 164 p.

Badran, M.M.M., 2009. Petrology and uranium potentiality of Gabal El-Mueilha granitoids and other associated rocks, South Eastern Desert, Egypt. M.Sc. Thesis, Fac. Sci., Azhar Univ., Cairo, Egypt, 171p.

Bentor, Y.K., 1985. The crustal evolution of the Arabo-Nubian massif with special reference to the Sinai Peninsula. Precamb. Res. ,28 (1), 1–74.

Dawoud, M.; Abdel Ghani, I.M.; Elsaid, M., and Badr, Y.S., 2017. The Integration of ASTER

Imagery and Airborne Gamma-ray Spectrometry in Lithological Discrimination of Ras Barud - Um Tagher Area, North Eastern Desert, Egypt. Inter. J. Innovative Sci., Engineering & Technology, 4 (9), 9-23.

Deer, W.A.; Howie, R.A., and Zussman, J., 1992. An introduction to the rock forming minerals. 2nd ed., Longman, London, 696 p.

Duval, J.S., 1983. Composite colour images of aerial gamma-ray spectrometric data. Geophysics, 48, 722-735.

El Mansi, M.M., 1996. Petrology and mineralogy of Samut-Atud area, Central Eastern Desert, Egypt. Ph. D. Thesis. Fac. of Sci., Cairo Univ., 320 P.

El Mansi, M.M., 2000. Colouration of fluorite and its relation to radioactivity. Egypt. Mineralogist, J. Mineral. Soci. Egypt, 12, 93-106.

Elawadi, I.A.; Ammar, A.A., and Elsirafy, A., 2004. Mapping surface geology using airborne gamma-ray spectrometric survey data- a case study. Proc. The 7th SEGI inter. Symp.-Imaging Technology, Sendai, Japan, 349-354.

Eliwa, H.A.; Kimura, J.I., and Itaya, T., 2006. Late Neoproterozoic Dokhan Volcanics, North eastern Desert, Egypt; geochemistry and petrogenesis. Precambrian Research, 151, 31 –52.

El-Ramly, M.F., and Al-Far, D.M., 1955. Geology of El-Mueilha-Dungash district. Artic. Geol. Surv. Egypt., 44p.

Elsirafy, A.M.; Maleik, M.L., and Aref, A.A., .1999. Utilization of remotely sensed spectral gamma-ray survey data in mineral exploration: Gabal Amrit area, South Eastern Desert, Egypt. 1th Seminar on raw Nuclear Materials and Their Technologies, NMA-Cairo, Egypt, November 1-3., 1-22.

Fouad, K.M.; Mielik, M.L., and Gharieb, A.N., 2004. An attempt to automate the lithological classification of rocks using geological, gamma-spectrometric and satellite image datasets. 7th Arab Conf. peaceful uses of Atomic Energy, Sanaa, 4-8 Decembe, 1-16.

Grasty, R.L., and Shives, R.B.K., 1997. Applications of gamma ray spectrometry to mineral exploration and geological mapping, Workshop presented at Exploration 97. 4th Decennial Conf. Mineral Exploration.

Greenberg, J.K., 1981. Characteristics and origin of Egyptian Younger Granites: summary. Geol. Soc. Amer. Bulletin, 92, 224 –232.

Hassan, M.A., and Hashad, A.H., 1990. Precambrian of Egypt. In: The Geology of Egypt (Said, R.,Ed.). Balkema, Rotterdam, 201–245.

Hyvönen, E.; Turunen, P.; Vanhanen, E.; Arkimaa, H., and Sutinen, R., 2005. Airborne gamma-ray surveys in Finland. Geol. Sur. Finland, Special Paper 39, 119–134.

Johnson, P.R., 1998. Tectonic map of Saudi Arabia and adjacent areas. Saudi Arabian Deputy Ministry for Mineral Resource, Technical Report USGS-TR-98-3, (scale 1: 40,000,000).

Johnson, P.R.; Andresen, A.; Collins, A.S.; Fowler, A.R.; Fritz, H.; Ghebrab, W.; Kusky, T., and Stern, R.J., .2011. Late Cryogenian-Ediacaran history of the Arabian-Nubian Shield: a review of depositional, plutonic, structural, and tectonic event in the closing stages of the northern East African Orogen. J. African Earth Sciences, 61, 167–23 2

Khamies, A.M., and Terras, M.M., .2009. surface and subsurface structures of Kalabsha area, southern Egypt, from remote sensing, aeromagnetic and gravity data. Egypt J. Remote Sensing & Space., 13, 1-15.

Kröner, A., 1985. Ophiolites and the evolution of tectonic boundaries in the late Proterozoic Arabian–Nubian Shield of northeastern Africa and Arabia. Precambrian Research, 27, 277–300.

Moussa, E.M.M.; Stern, R.J.; Manton, W.I., and Ali, K.A., 2008. SHRIMP zircon dating and Sm/Nd isotopic investigations of Neoproterozoic granitoids, Eastern Desert, Egypt. Precamb. Res., 160,341 – 356.

Nash, J.T., 1979. Uranium and thorium in granitic rocks of north-eastern Washington and northern Idaho, with comments on uranium resource potential. U.S. Geol. Sur. Open-File Rept., 79–233, 39.

Obeid, M.; Ali, M., and Mohamed, N., 2001. Geochemical Exploration on the Stream Sediments of Gabal El Mueilha Area, Central Eastern Desert, Egypt: An Overview on the Rare Metals. Resource Geology, 51(3), 217–227.

Omran, A.A., and Dessouky, O.K., .2016. Ra's Abdah of the north-Eastern Desert of Egypt: the role of granitic dykes in the formation of radioactive mineralization, evidenced by zircon morphology and chemistry. Acta Geochim, 35(4),368–380.

Peterson, J., and Eliasson, J., 1997. Mineral evolution and element mobility during episyenitization and albitization in the Bohus granites, Sweden . Lithos., 42, 123-146.

Quick, J.E., 1991. Late Proterozoic transpression on the Nabitah fault system-implications for the assembly of the Arabian Shield. Precambr. Res., 53,119–147

Raslan, M.F., 2009. Mineralogical and geochemical characteristics of uranium-rich fluorite in El-Missikat mineralized granite, Central Eastern Desert, Egypt. Geologija., 52/2, 213-220.

Read, H.H., 1984. Rutley's elements of mineralogy. Published by S.K. Jam for CBS Publishers and Distributors. Delhi, India., 560p.

Ries, A.C.; Shackleton, R.M.; Graham, R.H., and Fitches, W.R., 1983. Pan-African structures, ophiolites and mélange in the Eastern Desert of Egypt: a traverse at 26°N. J. Geol. Soc. London ,140, 75 –95.

Robinson, F.A.; Foden, J.D.; Collins, A.S., and Payne, J.L., 2014. Arabian Shield magmatic cycles and their relationship with Gondwana assembly: insights from zircon U–Pb and Hf isotopes. Earth and Planetary Science Letters, 408, 207–225

Samaan, J.M., 2009. Geology, petrology and radiometrical characteristics of Gabal El Mueilha A-type granites, Central Eastern Desert, Egypt. Proc. 1st Sympos. Geol. Resour. Tethys Realm, Cairo Univ., 123 – 130.

Soliman, M.M., 1981. Geochemical surveys of Sn, Nb, Cu and Au mineralizations, Mueilha-Dungash area, southeastern Desert, Egypt. Geol. Mag., GBR, 118, 545-549.

Stern, R.J., 1994. Arc assembly and continental collision in the Neoproterozoic East African Orogen: implications for the consolidation of Gondwanaland. Annual Review of Earth and Planetary Sciences ,22, 319–351.

Stern, R.J., and Hedge, C.E., 1985. Geochronologic and isotopic constraints on Late Precambrian crustal evolution in the Eastern Desert of Egypt. Am. J. Sci., 285, 97 –127.

Stern, R.J., and Johnson P.R., 2010. Continental lithosphere of the Arabian Plate: a geologic, petrologic, and geophysical synthesis. Earth Sci Rev., 101,29–67.

Stoeser, D., and Camp, E., 1985. Pan-African microplate accretion of the Arabian Shield. Geol. Soc. Amer. Bull., 96,817–826.

Streckeisen, A., 1976. To each plutonic rock its proper name, In Earth-Science Reviews, 12(1),1-33, ISSN 0012-8252.

Stuckless, J.S., 1979. Uranium and thorium concentrations in Precambrian granites as indicators of a uranium province in central Wyoming. Contrib. Geol., 17(2),173–178.

Vail, J.R., 1985. Pan-African (Late Precambrian) tectonic terrains and the reconstruction of the Arabian-Nubian Shield. Geology, 13,839–842.

Wilford, J.R., 1992. Regolith mapping using integrated Landsat TM imagery and high-resolution gamma-ray spectrometric imagery-Cape York peninsula. burreau of mineral Resources Record, 1992/78,35p.

المساهمة في جيولوجية وبترولوجية والمسح الطيفى الجوى لأشعة جاما لصخور جرانيتات جبل المويلحه، جنوب الصحراء الشرقية، مصر

إسماعيل محمد عبد الغنى

تظهر الصخور الجرانيتية الحديثة لجبل المويلحة على هيئة جسم بيضاوى يتداخل فى كل الصخور المحيطة به والتى تتكون من صخور الميلانج الأوفيوليتي والبركانيات المتحولة والجرانيتويدات القديمة والجابرو الحديث والتي تم فصلها حقلياً ورسم خطوط التماس بينها بدقة بالاستعانة بنتائج معالجة بيانات القمر الصناعى لاندسات8- والتي ساهمت أيضاً في تحديد أماكن وأنواع التغير والتحول بالمنطقة. ويرسل الجرانيت الحديث العديد من الأذرع داخل هذه الصخور المحيطة به خصوصاً صخور البركانيات القديمة. تتأثر المنطقة بالعديد من الصدوع في اتجاهات مختلفة أهمها في اتجاه (شمال غرب–جنوب شرق) و (شمال شرق-جنوب غرب) و (شمال-جنوب) والتى تتوافق مع معظم اتجاهات الأودية بالمنطقة مما يدل على أن معظم الأودية ذات طابع تركيبى.

بتروجرافيا، يتمثل الجرانيت الحديث بنوع واحد من السيانوجرانيت (جرانيت مسكوفيتي) والذي يتأثر بدرجات تحلل متفاوتة من عمليات الألبتة والتي تزداد عند الأطراف الخارجية للكتلة الجرانيتية وخصوصاً الجنوبية والجنوبية الغربية منها وكذلك على مستويات التصدع بالإضافة إلى التحلل والتغير بواسطة محاليل الحديد والسليكا. كما أوضحت الدراسات البتروجرافية والمعدنية لجرانيت جبل المويلحة أن أهم المعادن الزائدة (أو الإضافية) هى معادن الكاسيتريت والفلوريت والزركون والبيريل (الذي سجل لأول مرة في هذه الصخور) والمونازيت والثوريت واليورانوثوريت والتي يعزى إليها الشاذة الإشعاعية لهذه الكتلة الجرانيتية. وقد أظهر المسح الإشعاعي الجوى لأشعة جاما وجود شاذة إشعاعية كبيرة منحصرة فوق كتلة الجرانيت المحاط بصخور أخرى متوسطة وضعيفة إشعاعيا. وبحساب نسبة الثوريوم/اليورانيوم اتضح أن جرانيت جبل المويلحة قد تم له إثراء فى محتوى اليورانيوم المتواجد فيه وخاصة أثناء عمليات الألبتة.

ومن الجدير بالذكر أن معدن الكاسيتريت والفلوريت يتواجدان في صورة تمعدنات بالقرب من كتلة جرانيت جبل المويلحة الأساسية كما في منجم المويلحة للقصدير على بعد ثلاثة كيلومترات تقريباً إلى الشمال الغربى من جبل المويلحة وكذلك منجم أم ضلاليل للفلورين على بعد كيلومترين تقريباً شمال شرق جبل المويلحة كما أنَّ العلاقة الوثيقة لهذه التمعدنات بالكتلة الجرانيتية تشير إلى أن عمليات الصهارة وعمليات التغيير اللاحقة لعبت دورا مهما في تكوين هذه المعادن.